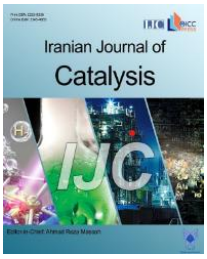

Iran. J. Catal. 2026; 16(1): 1-18

Iranian Journal of Catalysis (IJC)

https://doi.org/10.57647/ijc.2026.1601.01

Research Article

Green Synthesis of Zinc Oxide (ZnO) Nanoparticles Using *Madhuca longifolia* Flowers for Enhanced Photodegradation and Antibacterial Applications

Rahul Rameshcandra Bhavsar[1], Ravikiran Sukdeo Pagare[1], Sachin Girdhar Shinde[2,*], Maheshkumar Prakash Patil[3]

[1]*Research Centre, Department of Biological Science, School of Science, Sandip University, Nashik, Maharashtra, India*
[2]*Research Centre, K.V.N Nanik Arts, Commerce and Science College, Nashik, Affiliated to Savitribai Phule Pune University, Pune, Maharashtra, India*
[3]*Research Institute for Basic Sciences, Pukyong National University, 45 Yongsoro, Nam-gu, Busan, 48513, Republic of Korea*

[*] **Corresponding authors:** sachings93@gmail.com

Article History:

Received:
19 May 2025

Revised:
3 December 2025

Accepted:
18 December 2025

Published Online:
24 December 2025

Published in Issue:
31 March 2026

Abstract

The present study involves green synthesis of ZnO nanoparticles (NPs) using aqueous *Madhuca Longifolia* flower extract from hydrothermal synthesis. The ZnO NPs were characterized by X-ray diffraction (XRD), UV–visible studies, Transmission electron microscopy (TEM), FT-IR, SEM, and EDAX. The NPs were evaluated for photodegradative and antimicrobial activities. UV–visible absorption of ZnO NPs showed an absorption band at 356 nm, which can be assigned to an effective formation of ZnO NPs having appreciable activity in the visible range, confirmed by the Tauc plot showing a 3.21 eV band gap. TEM image confirms the formation of nanoparticles, and the average crystallite sizes were found to be 17-20 nm. Eosin Blue (EB) dye was effectively degraded under sunlight in the minimum quantity of ZnO NPs. Excellent bactericidal activity was shown by the NPs on Gram-positive (*Bacillus cereus* ATCC13061, *Staphylococcus saprophyticus* KCTC3345) and Gram-negative (*Escherichia coli* KCTC1682, *Salmonella typhimurium* KCCM11862) bacteria. Synthesis of multifunctional ZnO NPs using naturally occurring *M. longifolia* plant flower has been an excellent, cost-effective, and environmentally friendly alternative to chemical methods.

Keywords: Antimicrobial activity, Madhuca longifolia, Photocatalysis, ZnO nanoparticles

Cite this article: R. Rameshcandra Bhavsar, R. Sukdeo Pagare, S. Girdhar Shinde, M.Prakash Patil, Iran. J. Catal. **16** (2026) 1-18. https://doi.org/10.57647/ijc.2026.1601.01

1. Introduction

Dye effluents originating from textile, printing, and other industrial processes constitute a major source of environmental pollution. These persistent pollutants often infiltrate aquatic ecosystems, posing serious ecological and health hazards. Conventional wastewater treatment techniques such as osmosis, adsorption, and flocculation have been explored for dye removal, yet each exhibits inherent limitations in efficiency, cost, and sustainability [1, 2]. In contrast, photocatalytic degradation has emerged as an environmentally benign, cost-effective, and highly efficient strategy for eliminating such contaminants. Among various photocatalysts, zinc oxide (ZnO) has received considerable attention for the photodegradation of organic pollutants [3].

Beyond environmental remediation, microbial contamination has become a critical challenge in

healthcare, food, and water systems, necessitating the development of effective antimicrobial materials and surface coatings [4,5]. The remarkable antimicrobial potential of metal oxide nanoparticles (NPs) has drawn increasing interest over the past decade [6,7].

In particular, nano-sized semiconductors exhibit superior photocatalytic activity owing to their large surface area and quantum confinement effects, which enhance charge carrier separation and reactivity. When irradiated with light of energy greater than their bandgap, these materials generate electron–hole (e^-/h^+) pairs that migrate to the surface and participate in redox reactions, producing reactive oxygen species (ROS) capable of degrading organic molecules and inactivating microbes [8–13].

ZnO, a well-established n-type semiconductor with a wide bandgap (~3.37 eV) and high exciton binding energy (~60 meV), stands out due to its strong redox potential, high electron mobility, photostability, and efficient charge separation [14]. Upon illumination, ZnO generates ROS, including hydroxyl (·OH) and superoxide ($O_2^{-}\cdot$) radicals, which oxidize dye molecules. Its large surface area enhances the adsorption of pollutants, while intrinsic defect sites promote charge transfer and suppress recombination, further improving photocatalytic efficiency. Additionally, the conduction band potential of ZnO (–0.5 V vs. NHE) favors oxygen reduction reactions, accelerating the overall degradation process. Structural modifications such as doping and nanostructuring structuring have also been reported to enhance activity by extending visible-light absorption and reducing electron–hole recombination [15,16]. Numerous synthetic approaches, including sol–gel, solvothermal, co-precipitation, and hydrothermal techniques, have been reported for the preparation of ZnO nanostructures [17]. However, these conventional routes often involve toxic metal precursors, hazardous organic solvents, and energy-intensive conditions, which generate harmful by-products, increase environmental burden, and raise safety concerns [18]. Moreover, nanoparticle aggregation and the need for stabilizing agents further limit their reproducibility and scalability. In contrast, green synthesis, particularly using plant extracts, offers an eco-friendly, simple, and cost-effective alternative. Phytochemicals such as alkaloids, flavonoids, terpenoids, and polyphenols act as natural reducing and capping agents, facilitating the formation of uniform, stable, and crystalline ZnO nanoparticles under mild reaction conditions [19–21]. In this study, we report the green hydrothermal synthesis of ZnO nanoparticles using *Madhuca longifolia* flower extract as a novel biological reductant and stabilizing agent. To the best of our knowledge, this is the first systematic exploration of *M. longifolia* flowers for nanoparticle synthesis. The extract is enriched with diverse bioactive compounds, including flavonoids (lutein, quercetin, myricetin, rutin) and phenolic acids (vanillic, protocatechuic, gallic, ferulic, caffeic), which provide multiple hydroxyl and aromatic groups that serve as electron donors during Zn^{2+} reduction and as capping agents for nanoparticle stabilization [22,23].

These phytoconstituents influence crystal nucleation and growth kinetics, suppress agglomeration, and fine-tune the surface morphology and defect chemistry of ZnO nanostructures. The resulting nanoparticles are expected to exhibit enhanced photocatalytic activity, attributable to improved charge separation and surface passivation, and superior antibacterial performance, due to increased surface reactivity and biofunctionalization [24].

Thus, this work establishes a sustainable, biogenic route for the fabrication of multifunctional ZnO nanoparticles with significant environmental and biomedical potential.

2. Materials and methods

2.1. Materials

Analytical-grade zinc nitrate hexahydrate ($Zn(NO_3)_2\cdot 6H_2O$) was procured from Merck India Ltd., Mumbai, India, and used without further purification. Fresh *Madhuca longifolia* flowers were collected directly from trees located in Molgi, Nandurbar District, Maharashtra, India.

The microbial growth media, Mueller–Hinton Broth (MHB) and Mueller–Hinton Agar (MHA), were obtained from Thermo Fisher Scientific India Pvt. Ltd., Powai, Mumbai. Ninety-six–well microdilution plates were purchased from Chargen Life Sciences LLP, Mumbai. All aqueous solutions were prepared using deionized water with a resistivity of 18.2 MΩ·cm.

2.2. Preparation of plant extract from *Madhuca longifolia* Flower

Madhuca longifolia (commonly known as Mahua) trees bloom during the months of March and April in the northern region of Maharashtra, India. The flowers are widely utilized by the indigenous tribal communities for food, fermentation, and medicinal purposes owing to their rich phytochemical composition. For the present study, mature and healthy flowers were freshly collected from *M. longifolia* trees located in Molgi, Nandurbar District (Maharashtra, India).

The collected samples were thoroughly washed with distilled water to remove dust and impurities and subsequently air-dried under shade in a well-ventilated environment to prevent the thermal and photolytic degradation of bioactive constituents. The drying process was continued for 8–10 days until complete removal of moisture.

10.57647/ijc.2026.1601.01

The dried flowers were then ground using a sterile mechanical grinder to obtain a homogeneous, fine aromatic powder, which was used for the preparation of the aqueous extract. Approximately 5.0 g of the powdered sample was dispersed in 100 mL of deionized water and heated in a thermostatic water bath at 70 °C for two h with gentle stirring to facilitate the extraction of thermally stable phytochemicals such as flavonoids, phenolic acids, and terpenoids. During extraction, the color of the solution gradually changed to light brown, indicating the release of water-soluble bioactive metabolites. After cooling to room temperature, the extract was filtered using Whatman No. 42 filter paper to remove any residual particulates. The resulting filtrate, rich in secondary metabolites capable of acting as reducing and capping agents, was stored in a sterile, cotton-plugged conical flask at 5 °C for subsequent synthesis of ZnO nanoparticles [25, 26].

2.3. Preparation of ZnO NPs from plant extract from *Madhuca longifolia* Flowers

Zinc oxide nanoparticles (ZnO NPs) were synthesized via a green hydrothermal-assisted route using an aqueous extract of *Madhuca longifolia* flowers as both a reducing and a capping agent. In a typical synthesis, 30 mL of 1 mM zinc nitrate hexahydrate ($Zn(NO_3)_2 \cdot 6H_2O$) solution was added dropwise to 5 mL of the prepared *M. longifolia* flower extract under constant magnetic stirring to ensure homogeneous mixing. The reaction mixture was maintained in a thermostatically controlled water bath at 50 °C for 30 min. During the reaction, a gradual color change from pale yellow to milky white was observed, accompanied by the formation of a white precipitate, indicating the nucleation and growth of ZnO nanoparticles.After completion of the reaction, the colloidal suspension was centrifuged at 9000 rpm for 30 min to separate the solid product. The obtained residue was repeatedly washed with deionized water and ethanol to remove unreacted precursors and residual organic compounds from the extract.

The purified material was then dried at 80 °C overnight in a hot-air oven, ground into a fine powder, and subsequently calcined at 350 °C in a muffle furnace at a heating rate of 10 °C min^{-1} for 2 h to achieve complete crystallization of ZnO nanoparticles.The formation of ZnO NPs was preliminarily confirmed by UV–Visible spectroscopy (Fig. 1).

The absorption spectrum of the *M. longifolia* flower extract exhibited a characteristic peak at 429 nm, while the synthesized ZnO NPs displayed a strong absorption band around 448 nm, corresponding to the intrinsic band-to-band transition of ZnO. This distinct blue shift in the absorption edge confirmed the successful formation of ZnO nanoparticles through the plant-extract-mediated hydrothermal route [27, 28].

2.4. Statistical analysis

All experimental measurements were conducted in triplicate (n = 3), and the results are presented as mean ± standard deviation (SD). The photocatalytic degradation efficiency and antibacterial activity data were statistically analyzed using one-way analysis of variance (ANOVA) followed by Tukey's post-hoc test to determine significant differences among experimental groups. Statistical analyses were performed using OriginPro 8.5 software, and differences were considered statistically significant at $p < 0.05$.

3. Results and discussion

3.1. Characterization

The synthesized ZnO nanoparticles were comprehensively characterized using a suite of advanced analytical techniques to elucidate their structural, morphological, optical, and compositional properties. X-ray diffraction (XRD) analysis was carried out using a diffractometer equipped with monochromatic Cu Kα radiation (λ = 1.5406 Å) operated at 45 kV and 40 mA to determine the crystalline phase, lattice structure, and average crystallite size. Data were collected at 25 °C over a 2θ range of 20°–90°, with a step size of 0.017° and a continuous scanning rate of 0.1° s^{-1}.Transmission electron microscopy (TEM) (Philips CM 200) was employed to examine the particle morphology, size distribution, and degree of agglomeration, while scanning electron microscopy (SEM) coupled with energy-dispersive X-ray spectroscopy (EDS) (JSM 7600F) provided detailed surface topography and elemental composition.To identify the functional groups involved in nanoparticle stabilization, Fourier-transform infrared (FT-IR) spectroscopy was performed using a Bruker Hyperion 3000 microscope coupled with a Vertex 800 FT-IR system in the range of 4000–400 cm^{-1}. The optical absorption and band gap characteristics of the nanoparticles were investigated using UV–Visible diffuse reflectance spectroscopy (UV-DRS) on a JASCO V-750 spectrophotometer equipped with an ISV-922 integrating sphere. Additionally, UV–Visible absorbance measurements were recorded using a JASCO V-730 double-beam spectrophotometer to monitor the photocatalytic degradation of Eosin Blue dye under sunlight irradiation.

3.2. UV-DRS analysis

The optical properties of the synthesized ZnO nanoparticles were investigated using UV–Visible diffuse reflectance spectroscopy (UV–DRS). As shown in Fig. 2, the ZnO nanoparticles synthesized from *Madhuca*

longifolia flower extract exhibited a distinct and intense absorption edge centered at 356 nm, which corresponds to the intrinsic band-to-band electronic transition of ZnO. This prominent absorption feature confirms the successful formation of nanoscale ZnO with characteristic semiconductor behavior.The inset Tauc plot (Fig. 2, inset) was used to estimate the optical band gap energy (E_9), which was calculated to be approximately 3.21 eV. This direct band gap value is in close agreement with reported literature for ZnO nanostructures and reflects a slight blue shift relative to bulk ZnO, attributable to the quantum confinement effect arising from nanoscale dimensions [29, 30]. The sharp and well-defined absorption edge further indicates a high degree of optical purity and crystallinity, suggesting minimal defect-induced absorption. The incorporation of *Madhuca longifolia* flower extract during synthesis likely contributed to improved nanoparticle stabilization, uniform size distribution, and surface passivation through the coordinated action of flavonoids and phenolic compounds. These biomolecules not only act as natural reducing and capping agents but also enhance the environmental compatibility of the synthesis process [31]. Overall, the UV–DRS analysis validates the successful green synthesis of highly crystalline ZnO nanoparticles with desirable optical properties, underscoring their suitability for photocatalytic and optoelectronic applications.

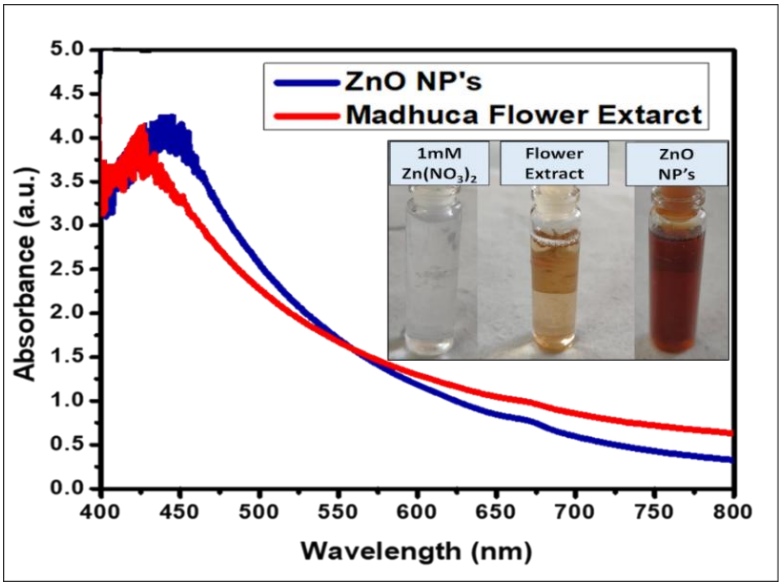

Figure 1. UV–Vis spectra of *Madhuca longifolia* extract and biosynthesized ZnO nanoparticles

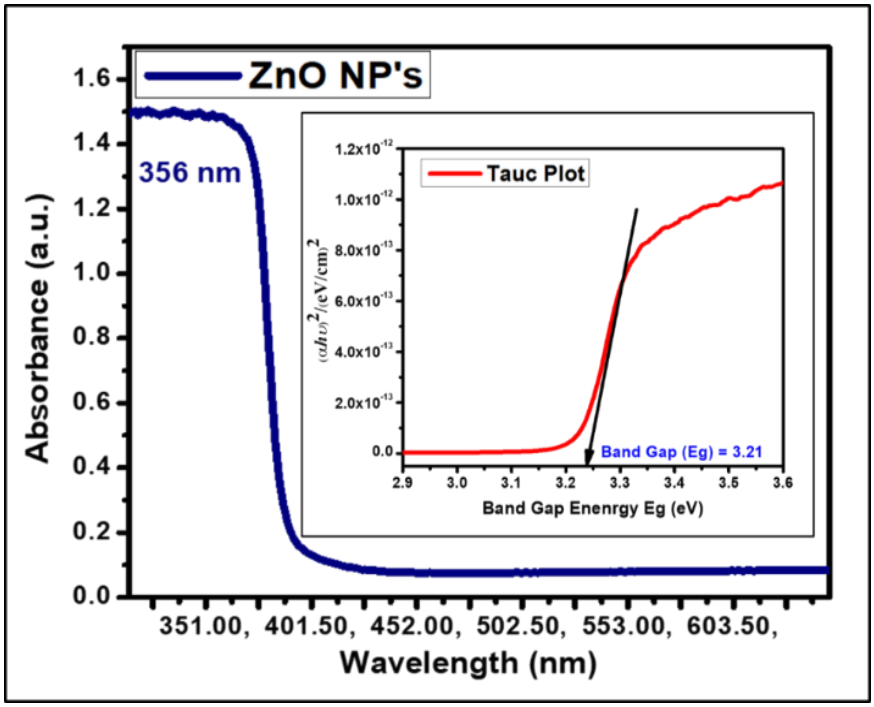

Figure 2. UV–DRS spectrum and corresponding Tauc plot of ZnO nanoparticles synthesized using *Madhuca longifolia* flower extract

10.57647/ijc.2026.1601.01

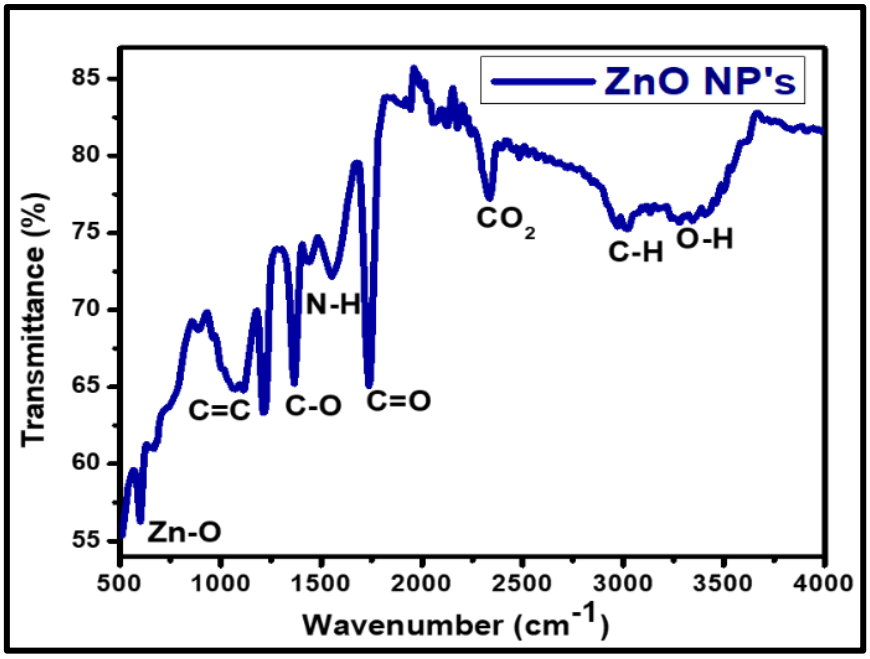

Figure 3. FT-IR spectrum of ZnO nanoparticles synthesized using *Madhuca longifolia* flower extract

3.3. FT-IR analysis

The Fourier-transform infrared (FT-IR) spectrum provides critical insights into the functional groups involved in the biosynthesis and stabilization of ZnO nanoparticles synthesized using *Madhuca longifolia* flower extract. As illustrated in Fig. 3, a prominent absorption band observed in the range of 500–600 cm^{-1} corresponds to the Zn–O stretching vibration, confirming the successful formation of ZnO nanoparticles [32].

Several additional absorption peaks are evident across the higher wavenumber regions, indicating the presence of various organic functional groups derived from the flower extract. The bands appearing between 1500–1700 cm^{-1} are attributed to C=C and C=O stretching vibrations, characteristic of aromatic rings and carbonyl compounds, respectively, which likely originate from flavonoids and phenolic acids acting as capping agents [33]. Peaks in the range of 1200–1400 cm^{-1} correspond to C–O stretching vibrations of alcohols, esters, or polyphenolic constituents, while a broad band observed between 3200–3600 cm^{-1} is associated with O–H stretching, indicative of hydroxyl groups involved in hydrogen bonding [34]. Additionally, weak bands in the region of 2800–3000 cm^{-1} are ascribed to C–H stretching vibrations, suggesting the presence of aliphatic compounds from the extract [35].

These spectral features collectively confirm that the phytochemicals present in *Madhuca longifolia* flower extract play a dual role: (i) reducing Zn^{2+} ions to ZnO and (ii) stabilizing the nanoparticles through surface adsorption of bio-organic moieties. The presence of these functional groups not only validates the green synthesis pathway but also highlights the eco-friendly, sustainable, and biocompatible nature of the process.

3.4. SEM and EDS analysis

The surface morphology of the synthesized ZnO nanoparticles was examined using scanning electron microscopy (SEM), and the corresponding micrograph is presented in Fig. 4a. The SEM image reveals that the ZnO nanoparticles synthesized using Madhuca longifolia flower extract exhibit predominantly spherical morphology, forming agglomerated clusters with noticeable porous structures. The hierarchical assembly of nanoparticles into micron-sized aggregates is evident from the scale bar (20 μm) and magnification (3.98 kx). The rough and irregular surface texture of the nanoparticles can be attributed to the adsorption of phytochemical constituents from the flower extract, which act as natural stabilizing and capping agents during the synthesis process. This biogenic interaction not only influences particle nucleation and growth but also contributes to the formation of mesoporous structures. Such structural features are advantageous for enhancing surface area and reactivity, making these ZnO nanoparticles highly suitable for photocatalytic and antibacterial applications [36].

The energy-dispersive X-ray spectroscopy (EDS) analysis further confirmed the elemental composition of the biosynthesized ZnO nanoparticles, as illustrated in Fig. 4b. The EDS spectrum exhibits strong and well-defined peaks corresponding to zinc (Zn) and oxygen (O), with their respective weight percentages of approximately 70.67% for Zn and 29.33% for O, confirming the successful formation of stoichiometric ZnO [37]. The absence of additional impurity peaks indicates the high purity of the nanoparticles, reflecting the effectiveness of the green synthesis route in minimizing contamination.

10.57647/ijc.2026.1601.01

The elemental mapping (highlighted in pink) demonstrates the uniform distribution of Zn and O across the analyzed region, further validating the homogeneity and compositional consistency of the sample. These findings substantiate the efficacy of the Madhuca longifolia-assisted green synthesis approach in producing high-purity, morphologically uniform ZnO nanoparticles with potential for diverse environmental and biomedical applications [38].

3.5. XRD analysis

The crystalline structure of the ZnO nanoparticles synthesized using *Madhuca longifolia* flower extract was examined by X-ray diffraction (XRD), and the corresponding diffraction pattern is presented in Fig. 5. The diffraction peaks observed at 2θ values corresponding to the (100), (002), (101), (102), (110), (103), (200), (112), (201), (004), and (202) planes can be well indexed to the hexagonal wurtzite phase of ZnO (JCPDS Card No. 36-1451). The calculated lattice constants (a = b = 3.249 Å and c = 5.206 Å) are in close agreement with the standard values reported for ZnO, confirming the formation of a single-phase crystalline structure.

The strong and sharp diffraction peaks corresponding to the (100), (002), and (101) planes indicate the high crystallinity and phase purity of the synthesized nanoparticles, demonstrating that the bio-mediated synthesis route effectively produced well-ordered ZnO crystallites [39–41].

The absence of any secondary or impurity peaks further supports the successful formation of pure ZnO nanoparticles without contamination from organic or metallic residues.

The average crystallite size (D) of the ZnO nanoparticles was calculated using Scherrer's equ. (1),

$$D = \frac{0.90\lambda}{\beta \cos\theta} \quad (1)$$

where K is the shape factor (0.9), λ is the X-ray wavelength (1.5406 Å), β is the full width at half maximum (FWHM) of the diffraction peak, and θ is the Bragg angle. Based on the intense (100), (002), (101), and (110) reflections, the average crystallite size was estimated to be approximately 17.31 nm, as summarized in Table 1 [42].

The narrow and intense diffraction peaks confirm the high degree of crystallinity, while the nanoscale crystallite size is consistent with quantum confinement effects observed in UV–DRS analysis. These results collectively validate the successful green synthesis of highly crystalline hexagonal wurtzite ZnO nanoparticles mediated by *Madhuca longifolia* flower extract.

3.6. TEM analysis

The morphological and structural characteristics of the synthesized ZnO nanoparticles were further examined using transmission electron microscopy (TEM), and the corresponding micrographs are presented in Figures 6a and 6b. The TEM images reveal that the ZnO nanoparticles synthesized using *Madhuca longifolia* flower extract exhibit irregular and slightly distorted spherical morphologies, forming agglomerated clusters of varying sizes. The scale bars of 200 nm and 50 nm confirm that the individual nanoparticles fall within the nanoscale dimension range, verifying their successful synthesis at the nanometer level.At higher magnification (50 nm scale), the nanoparticles display non-uniform and distorted spherical shapes, a feature commonly associated with biogenic synthesis routes, where phytochemicals from the plant extract influence the nucleation and growth kinetics of nanocrystals [44].

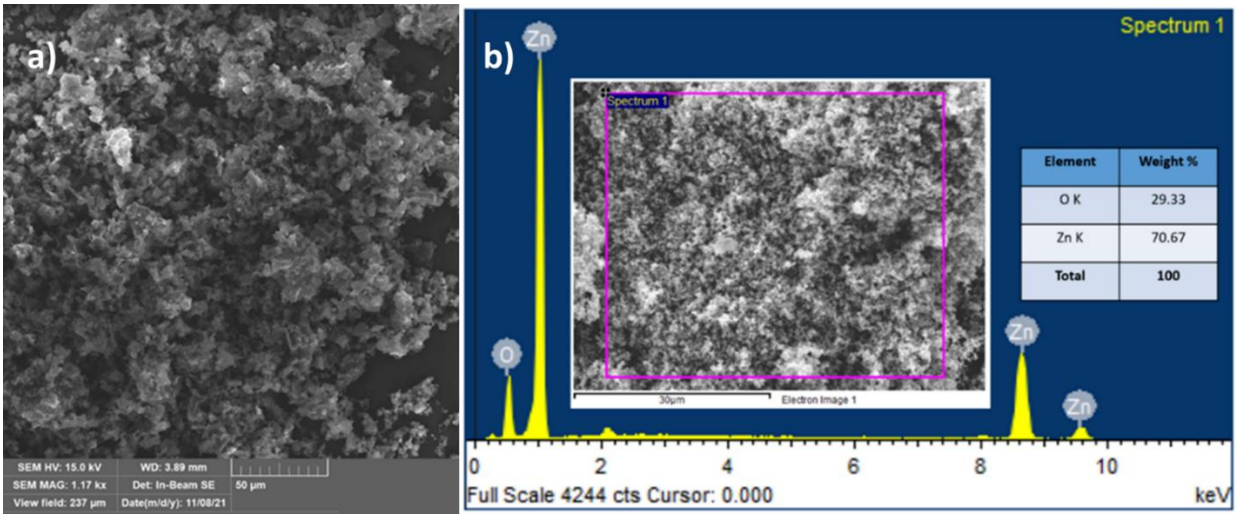

Figure 4. (a). SEM image of ZnO nanoparticles synthesized using *Madhuca longifolia* flower extract. (b). EDS spectrum of ZnO nanoparticles synthesized using *Madhuca longifolia* flower

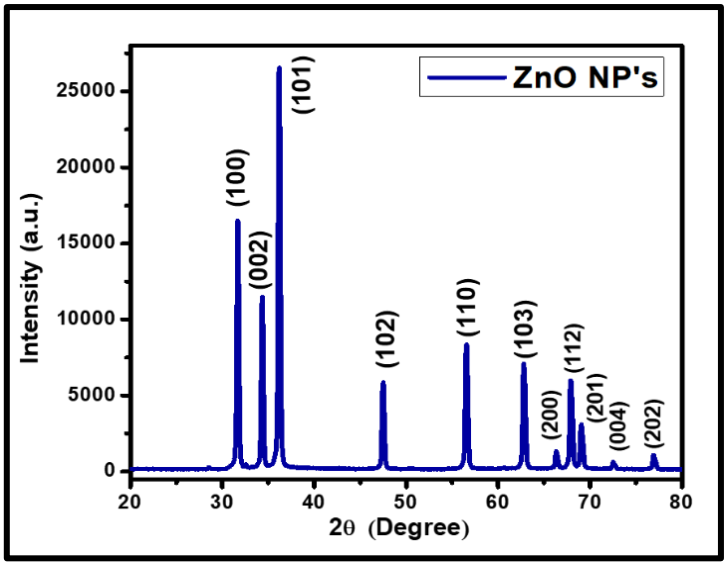

Figure 5. XRD pattern of ZnO nanoparticles synthesized using *Madhuca longifolia* flower extract

Table 1. Crystallite size parameters of ZnO nanoparticles synthesized using *Madhuca longifolia* flower extract

Peak position 2θ (°)	FWHM B_{size} (°)	Dp (nm)	Dp Average (nm)
(100)	0.401	21.56	
(002)	0.3998	21.78	17.31
(101)	1.1008	8.59	

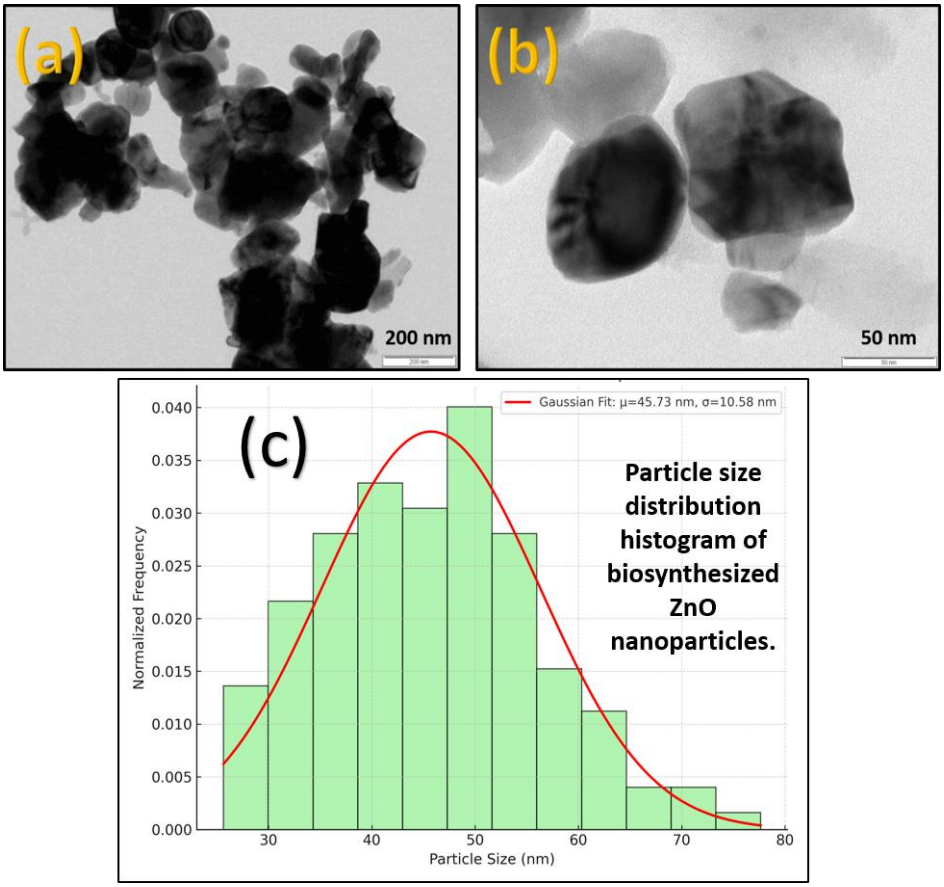

Figure 6. (a, b) TEM images and (c) particle size distribution histogram of ZnO nanoparticles synthesized using *Madhuca longifolia* flower extract

10.57647/ijc.2026.1601.01

The darker contrast regions in the micrograph correspond to densely packed crystalline domains, while the lighter regions represent less dense or amorphous zones, indicative of slight variations in particle packing and crystallinity.

The observed morphology reflects the dynamic interplay between the reducing and capping biomolecules present in the *Madhuca longifolia* extract such as flavonoids and phenolic acids, which govern the rate of crystal growth, surface stabilization, and aggregation. This results in ZnO nanoparticles with a distinct surface topology and structural heterogeneity.

Overall, the TEM observations confirm that the green synthesis route is not only simple and environmentally benign but also capable of producing stable ZnO nanoparticles with unique morphological characteristics, making them promising candidates for photocatalytic and biomedical applications. The particle size distribution histogram (Fig. 6(c)) illustrates the nanoscale dimensional characteristics of the biosynthesized ZnO nanoparticles.

The distribution follows a near-Gaussian profile, with particle sizes ranging from approximately 25 to 80 nm and an average diameter of around 45 nm. The relatively narrow spread indicates uniform nucleation and controlled growth of nanoparticles, governed by the phytochemical constituents of *Madhuca longifolia* extract acting as reducing and capping agents. The dominance of medium-sized particles within the distribution suggests effective stabilization during biosynthesis, minimizing excessive agglomeration or secondary growth. This size uniformity is advantageous for photocatalytic and antimicrobial applications, where surface area and charge carrier dynamics are strongly size-dependent [45].

3.7. Photocatalytic studies

The photocatalytic activity of the biosynthesized ZnO nanoparticles was evaluated under natural solar irradiation to emphasize the sustainability and eco-friendliness of the process. The experiments were conducted during periods of maximum solar intensity, characteristic of the Indian subcontinent's summer season. Specifically, photocatalytic degradation studies were performed in May, when solar radiation is most intense in central India. All experiments were carried out between 12:00 PM and 3:00 PM on clear, sunny days to ensure consistent light exposure and minimize spectral variation.

The average solar irradiance during the experiments was monitored using a calibrated digital solar power meter, and the recorded solar flux ranged between 850 and 1024 $W \cdot m^{-2}$ over the three-hour experimental period. The photocatalytic reaction assemblies were placed in open sunlight at a fixed distance to achieve uniform illumination across all samples. Various experimental parameters including pH, catalyst dosage, initial dye concentration, and reaction time were systematically optimized to evaluate their influence on photocatalytic efficiency. The experimental design and results for each parameter are discussed in the subsequent sections.

Upon sunlight irradiation, the ZnO nanoparticles absorb photons with energy equal to or greater than their band gap, leading to the excitation of electrons (e^-) from the valence band (VB) to the conduction band (CB), thereby generating electron–hole (e^-/h^+) pairs. The photogenerated electrons in the CB react with dissolved oxygen molecules to produce superoxide radicals ($\bullet O_2^-$), while the holes in the VB oxidize surface-adsorbed water or hydroxide ions to form hydroxyl radicals (•OH). These reactive oxygen species act as strong oxidizing agents that attack and decompose Eosin Blue dye molecules into smaller intermediates, which are further mineralized into CO_2, H_2O, and other harmless by-products.

The overall process thus involves efficient charge separation and radical-mediated oxidation, highlighting the photocatalytic efficiency of the biosynthesized ZnO nanoparticles under solar irradiation.

3.7.1. *Effect of pH of solution*

The pH of the dye solution is a key factor influencing the photocatalytic performance of semiconductor materials, as it directly affects surface charge, pollutant adsorption, and reactive species formation. Prior to photocatalytic evaluation, the point of zero charge (pH_pzc) of the synthesized ZnO nanoparticles was determined using a 1 M NaCl electrolyte by monitoring the pH variation of the suspension over a 48-hour equilibration period [46]. The pH_pzc of the ZnO photocatalyst was found to be approximately 7.3 (pH_pzc = 7.3). At this pH, the photocatalyst surface carries a net zero charge; below this value, it becomes positively charged, whereas at pH values above 7.3, it acquires a negative charge [47,48].

This surface charge behavior implies that higher photocatalytic degradation efficiency can be achieved at solution pH values lower than pH_pzc, where the positively charged catalyst surface promotes stronger electrostatic attraction and adsorption of negatively charged Eosin Blue (EB) dye molecules, thereby enhancing the overall photocatalytic reaction.

The influence of pH on the photocatalytic performance of ZnO nanoparticles is presented in Fig. 7. The catalyst exhibited optimal degradation efficiency at a slightly basic pH (pH = 8), despite a potential reduction in dye adsorption at higher pH. The reduced performance under acidic conditions can be attributed to the partial dissolution of ZnO in acidic media, leading to a loss of active sites [49].

In contrast, neutral to mildly alkaline environments favor photocatalytic activity due to enhanced generation of hydroxyl radicals and superoxide anions [50]. Beyond

pH 8, a decline in degradation efficiency was observed, likely caused by the reduced generation of reactive oxygen species (ROS), scavenging of •OH radicals by carbonate and bicarbonate ions formed from CO_2, and self-quenching via radical–radical recombination reactions [51].

To further understand the colloidal and surface characteristics of the ZnO nanoparticles, Zeta Potential analysis was performed (Fig. 8). The ZnO NPs exhibited a mean Zeta Potential of –7.96 mV with a Zeta Deviation of 6.18 mV, suggesting moderate colloidal instability and limited electrostatic repulsion between particles.

The conductivity of the colloidal dispersion was recorded as 0.00985 S/m, and the overall measurement quality was rated as *good*, confirming data reliability. The narrow distribution width (6.18 mV) indicates minimal variation in surface charge across particles.

These findings suggest that the ZnO nanoparticles possess a weak surface charge, which may favor controlled aggregation while maintaining sufficient interparticle interaction for photocatalytic activity. Understanding such surface charge dynamics is crucial for tailoring ZnO nanoparticles in photocatalytic, biomedical, and nanocomposite applications, where dispersion stability and surface reactivity govern performance outcomes [52].

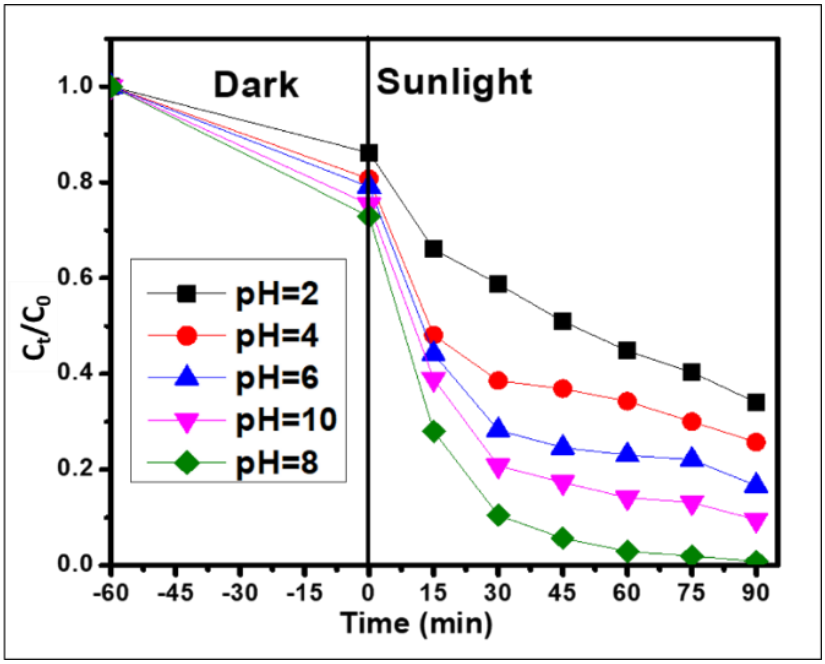

Figure 7. Effect of pH on the sunlight-driven photodegradation of Eosin Blue dye using ZnO nanoparticles (catalyst: 0.4 mg/100 mL; dye concentration: 10 mg/L)

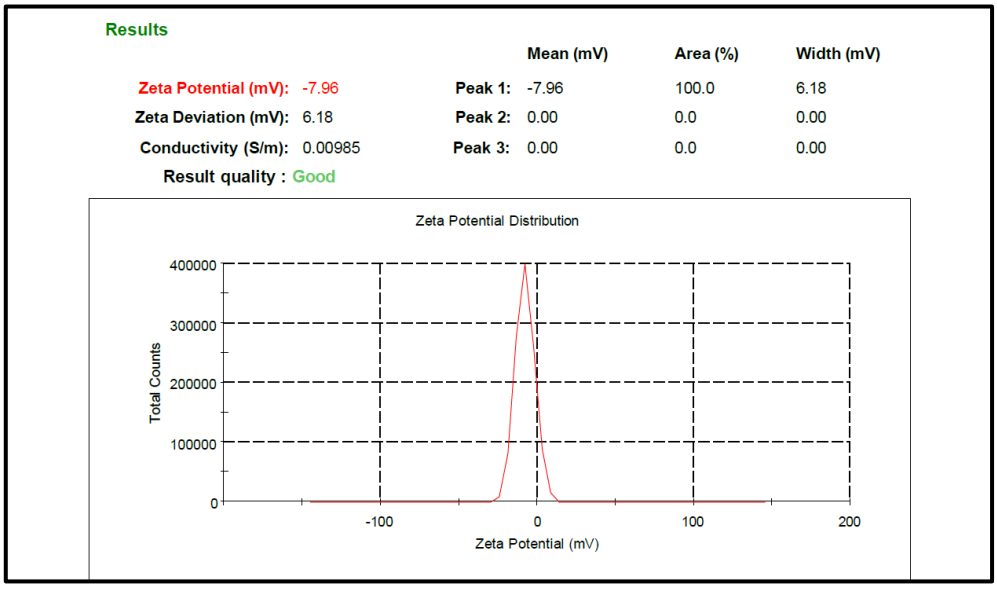

Figure 8. Zeta potential profile of ZnO nanoparticles synthesized using *Madhuca longifolia* flower extract

10.57647/ijc.2026.1601.01

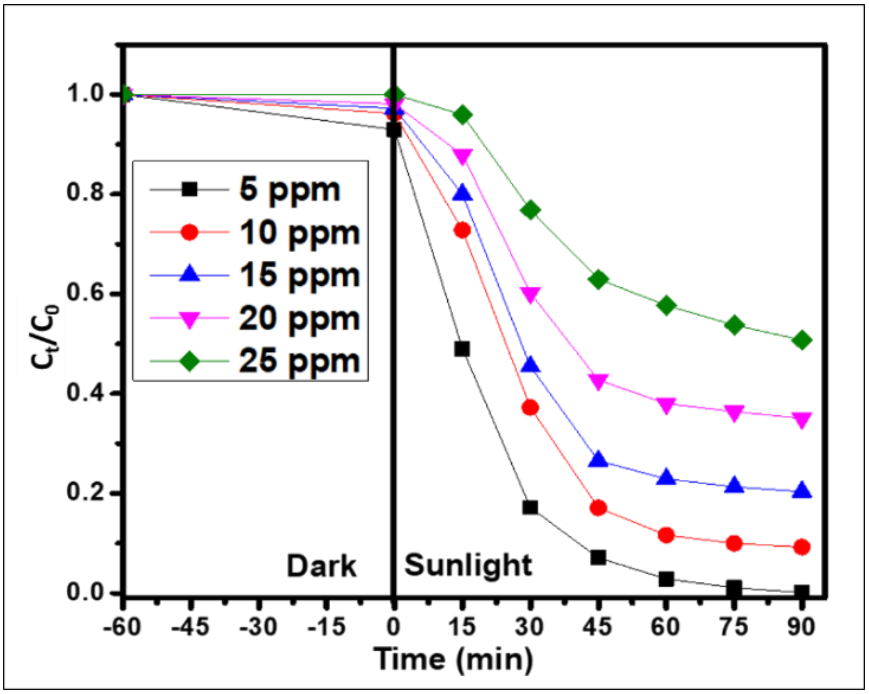

Figure 9. Effect of Eosin Blue dye concentration on its photodegradation under sunlight using ZnO nanoparticles (catalyst: 4 mg/100 mL; pH: 8.0)

3.7.2. *Effect of initial dye concentration*

The influence of the initial dye concentration on the photocatalytic degradation efficiency of ZnO nanoparticles was systematically examined under optimized conditions (pH = 9) by varying the Eosin Blue (EB) concentration from 10 to 30 mg·L^{-1} (Fig. 9). A series of 100 mL dye solutions were prepared by serial dilution, and the pH was precisely adjusted to 9 using 0.1 N HCl and 0.1 N NaOH solutions. The photocatalytic experiments were carried out by introducing 4 mg of ZnO nanoparticles per 100 mL of dye solution, and the mixtures were exposed to direct solar irradiation.

As shown in Fig. 9a, the absorbance intensity of EB decreased progressively with time, confirming continuous degradation of the dye under solar illumination. However, a noticeable decline in photocatalytic efficiency was observed with increasing initial dye concentration. The degradation percentage decreased as dye concentration increased from 10 to 30 mg·L^{-1}. This inverse correlation can be explained by several concurrent effects: (i) higher dye concentrations increase the optical density of the solution, restricting photon penetration to the catalyst surface; (ii) excessive dye molecules compete for the limited active sites on ZnO, reducing the adsorption of hydroxyl ions and dissolved oxygen necessary for the generation of reactive oxygen species (ROS) such as •OH and O_2^{-}•; and (iii) light attenuation within the bulk solution decreases the effective excitation of the catalyst, thereby lowering ROS generation rates [53,54].

Consequently, at higher dye concentrations, the probability of recombination between photogenerated electron–hole pairs increases, leading to diminished photocatalytic performance. In contrast, at lower dye concentrations (10 mg·L^{-1}), sufficient photon flux reaches the catalyst surface, maximizing charge separation and ROS formation, thus achieving higher degradation efficiency. The optimal operating conditions for maximum EB dye degradation were determined to be pH 8, catalyst dosage of 2 mg·100 mL^{-1}, and initial dye concentration of 10 mg·L^{-1} under solar radiation.

3.7.3. *Effect of catalyst dose*

The influence of catalyst dosage on the photocatalytic degradation of Eosin Blue (EB) dye was examined by maintaining the pH at 9 and the initial dye concentration at 10 mg·L^{-1}. As shown in Fig. 10, the degradation efficiency increased with catalyst loading up to an optimal dosage of 4 mg·100 mL^{-1}, beyond which a decline in performance was observed. The enhanced activity at lower dosages can be attributed to the increased number of active sites available for photon absorption and dye molecule interaction, thereby accelerating the generation of reactive oxygen species (ROS). However, further increasing the catalyst concentration above the optimal value resulted in a decrease in photocatalytic efficiency. This reduction can be attributed to particle agglomeration and incomplete dispersion of the catalyst in the reaction medium, even under vigorous stirring. The saturation of catalyst particles leads to light scattering and decreased penetration of solar radiation, consequently lowering photon absorption by the active sites and hindering ROS formation [50,55]. In addition, excessive catalyst concentrations may shield active sites from light exposure, thereby suppressing photocatalytic activity.

The color fading sequence during the degradation of EB dye under optimal conditions is illustrated in Fig. 11. The reaction was performed at pH 8, catalyst dosage of 4 mg·100 mL^{-1}, and initial dye concentration of 10 mg·L^{-1}. Under these conditions, the EB dye was almost completely degraded within 90 minutes of solar irradiation, achieving an impressive 97% degradation efficiency.

This result demonstrates the high photocatalytic activity and effectiveness of the plant-mediated ZnO nanoparticles, validating their potential for sustainable wastewater treatment and environmental remediation applications.

3.7.4. *Reusability of synthesized photocatalyst*

The stability and reusability of the biosynthesized ZnO photocatalyst were evaluated through consecutive photocatalytic degradation cycles under identical experimental conditions. Following each degradation run (first cycle), the treated dye solution was filtered using Whatman filter paper to recover the photocatalyst.

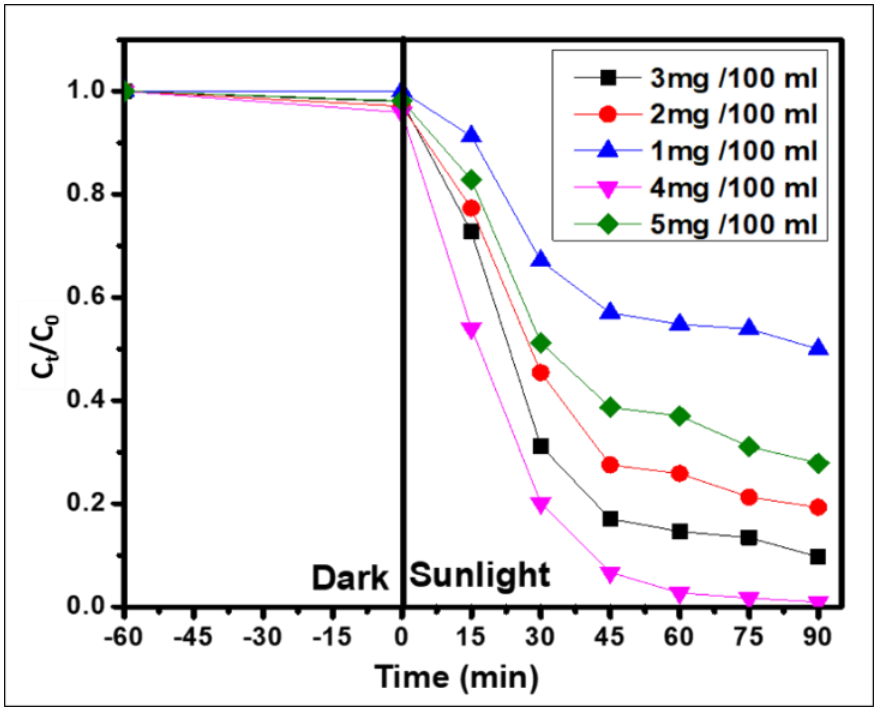

Figure 10. Effect of ZnO nanoparticle catalyst loading on the sunlight-induced photodegradation of Eosin Blue dye (dye concentration: 10 mg/100 mL; pH: 8.0)

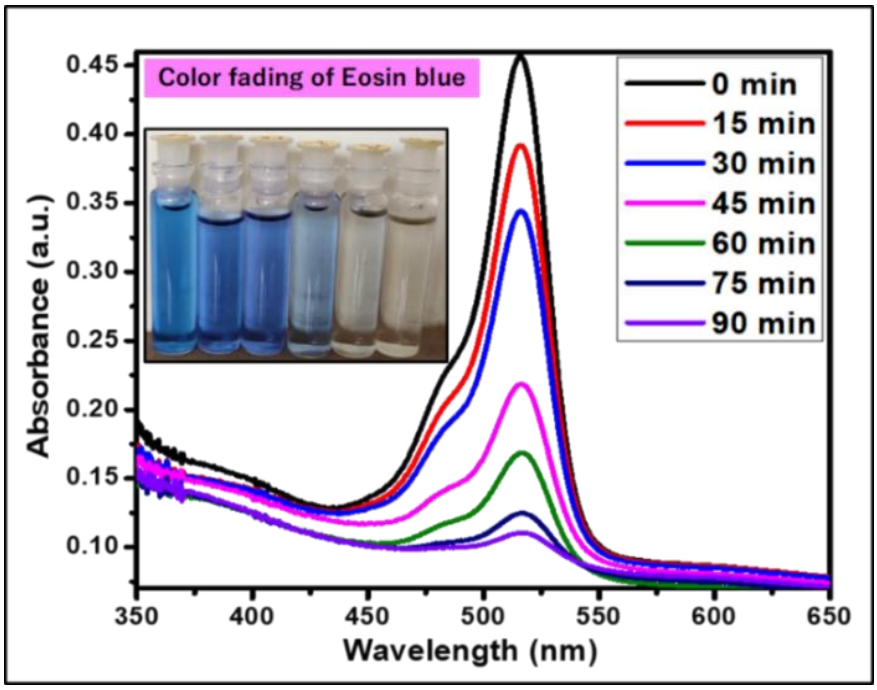

Figure 11. Sequential color fading of Eosin Blue dye under sunlight (catalyst loading: 4 mg/100 mL; pH: 8.0; dye concentration: 10 mg/100 mL)

10.57647/ijc.2026.1601.01

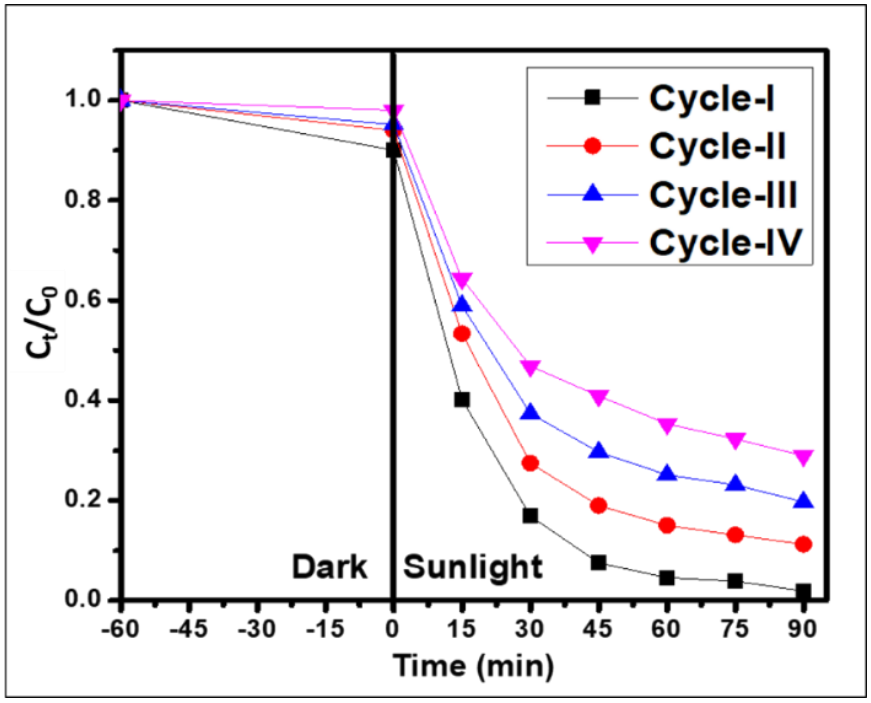

Figure 12. Reusability performance of ZnO nanoparticles for Eosin Blue dye photodegradation under sunlight (catalyst loading: 4 mg/100 mL; pH: 8.0; dye concentration: 10 mg/L)

The recovered catalyst was thoroughly washed with distilled water and ethanol to remove any residual dye or organic impurities, followed by drying in a hot-air oven at 150 °C for 2 hours to ensure complete removal of moisture and reactivation of surface sites [56].

The regenerated ZnO nanoparticles were subsequently reused for successive photocatalytic cycles under the optimized conditions of pH 8, catalyst dosage of 4 mg·100 mL^{-1}, and initial dye concentration of 10 $mg \cdot L^{-1}$ for the degradation of Eosin Blue (EB) under solar irradiation. As shown in Fig. 12, the catalyst maintained high photocatalytic efficiency for up to three consecutive cycles, exhibiting only a marginal reduction in degradation performance. After the fourth cycle, a slight decrease of approximately 7% in degradation efficiency was observed, indicating minor catalyst deactivation.

The observed decline in performance after multiple cycles may be attributed to partial loss of catalyst mass during the recovery process and deactivation of active surface sites due to dye molecule adsorption or surface fouling [57,58]. Nonetheless, the catalyst retained a substantial portion of its photocatalytic activity even after repeated use, demonstrating excellent stability, reusability, and structural robustness. These results confirm the potential of the plant-extract-mediated ZnO nanoparticles as a durable and cost-effective photocatalyst for sustainable wastewater treatment applications.

3.8. Antibacterial activity

The agar well diffusion method was employed to evaluate the antibacterial potential of the green-synthesized ZnO nanoparticles (ZnO NPs) following a standardized protocol [59]. Bacterial strains were procured from the Korean Culture Center of Microorganisms (KCCM), South Korea, and included two Gram-positive species—*Bacillus cereus* (ATCC 13061) and *Staphylococcus saprophyticus* (KCTC 3345)—and two Gram-negative species—*Escherichia coli* (KCTC 1682) and *Salmonella typhimurium* (KCCM 11862).

A standardized bacterial suspension was prepared by adjusting overnight-grown cultures to an optical density (OD_{600}) of 0.08–0.1 in sterile saline using a spectrophotometer (Libra S22, Biochrom Ltd., Cambridge, UK). Aliquots of 100 µL of each bacterial suspension were uniformly spread on Mueller–Hinton Agar (MHA) plates (BD Diagnostics, France) using a sterile L-shaped spreader. Wells of 8 mm diameter were bored aseptically into the agar using a sterile cork borer, and 100 µL of ZnO NP suspensions at varying concentrations (250, 500, 750, and 1000 $\mu g \cdot mL^{-1}$) were introduced into each well. Plates were incubated at 37 °C for 24 hours, and the zones of inhibition (ZOI) were measured in millimeters. The agar well diffusion assay was performed using gentamicin (10 µg/mL) as the positive control and sterile distilled water as the negative control to confirm that the observed zones of inhibition were specifically due to the activity of the biosynthesized ZnO nanoparticles. All experiments were performed in triplicate (n = 3), and results are reported as mean ± standard deviation (SD). Statistical evaluation using one-way ANOVA revealed a significant difference ($p < 0.05$) in antibacterial activity across the tested concentrations, confirming the dose-dependent inhibitory effect of ZnO

NPs. As illustrated in Fig. 13, the antibacterial efficacy of ZnO NPs increased progressively with concentration. At 1000 μg·mL^{-1}, the nanoparticles exhibited the largest ZOI, indicating maximum antibacterial effectiveness. Notably, Gram-positive bacteria (*B. cereus* and *S. saprophyticus*) showed larger inhibition zones compared to Gram-negative bacteria (*E. coli* and *S. typhimurium*), which is consistent with their structural differences. *E. coli* demonstrated the smallest inhibition zones across all concentrations, suggesting a higher degree of resistance to ZnO NPs.

The antibacterial mechanism of ZnO NPs is primarily attributed to the generation of reactive oxygen species (ROS), such as hydroxyl radicals (•OH) and superoxide ions (O_2^-•), along with the release of Zn^{2+} ions, which collectively induce oxidative stress, membrane disruption, and protein denaturation in bacterial cells [60,61]. Increased NP concentration enhances ROS generation, leading to more pronounced antibacterial effects [62,63]. The differential susceptibility among bacterial strains arises from variations in cell wall architecture. Gram-negative bacteria possess an additional lipopolysaccharide outer membrane, which serves as a diffusion barrier and imparts greater resistance, whereas Gram-positive bacteria lack this protective layer, rendering them more vulnerable to oxidative and ionic stress induced by ZnO NPs [64,65]. The observed antibacterial activity aligns with earlier findings [66], confirming that ZnO nanoparticles exhibit broad-spectrum antimicrobial potential, albeit requiring higher concentrations than silver nanoparticles to achieve comparable inhibition. Overall, these results demonstrate that the plant-mediated ZnO nanoparticles synthesized using *Madhuca longifolia* flower extract possess potent, concentration-dependent antibacterial activity, particularly against Gram-positive bacterial strains, establishing their promise for biomedical and antimicrobial coating applications.

3.9. Photocatalytic and antibacterial mechanisms

The proposed mechanism for the photocatalytic and antibacterial performance of ZnO nanoparticles (ZnO NPs) synthesized using *Madhuca longifolia* flower extract is illustrated in Fig. 14. When exposed to solar or UV irradiation, the semiconductor nature of ZnO NPs facilitates photoexcitation of electrons from the valence band (VB) to the conduction band (CB), leaving behind corresponding holes (h^+) in the VB. This process generates electron–hole (e^-/h^+) pairs, which migrate to the nanoparticle surface and initiate a cascade of redox reactions. At the surface, photogenerated electrons (e^-) react with adsorbed oxygen molecules to form superoxide radicals (O_2^-•), while holes (h^+) oxidize surface-bound hydroxyl ions (OH^-) or water molecules to produce hydroxyl radicals (•OH). These reactive oxygen species (ROS) including •OH, O_2^-•, and H_2O_2 are highly oxidative and non-selective, enabling the degradation of Eosin Blue (EB) dye molecules into simpler, non-toxic compounds such as CO_2 and H_2O [67]. The biomolecules present in the *M. longifolia* extract, rich in flavonoids and phenolic acids, act as both reducing and capping agents during synthesis, resulting in smaller, more stable ZnO NPs with enhanced surface area and defect density. This enlarged surface area provides a greater number of active sites for light absorption and pollutant adsorption, thereby amplifying ROS generation and ensuring efficient dye degradation. The intimate contact between dye molecules and the catalyst surface further accelerates redox reactions, contributing to the rapid photodegradation of EB under solar irradiation.

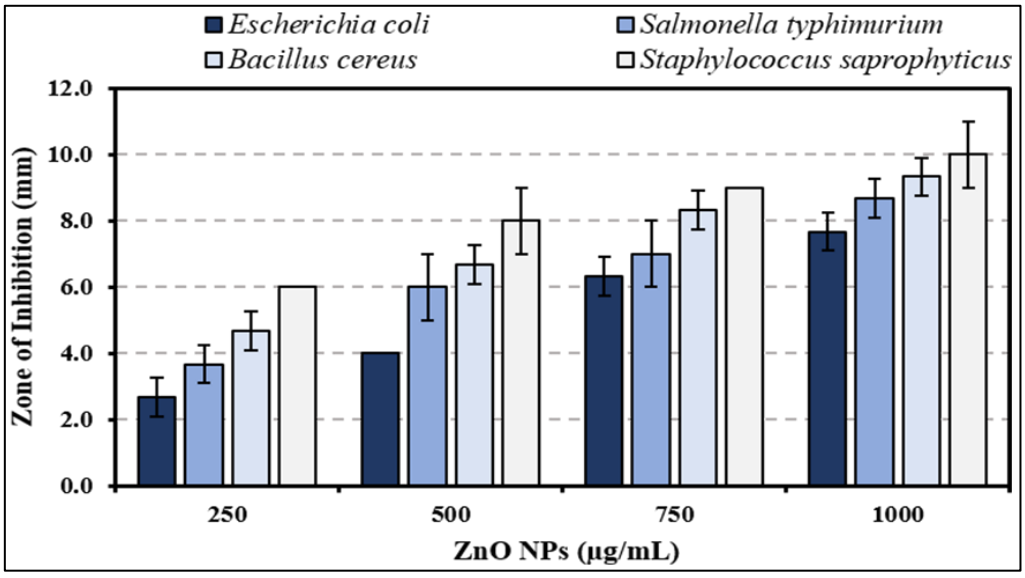

Figure 13. Antibacterial activity of *Madhuca longifolia* flower extract–mediated ZnO nanoparticles against pathogenic bacteria (data presented as mean ± SD, n = 3)

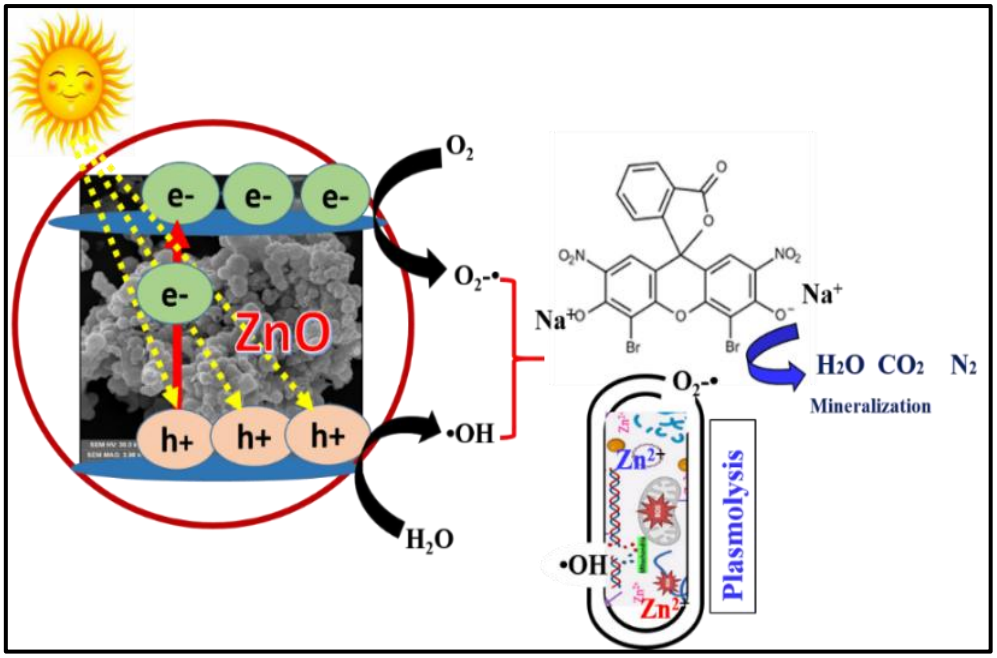

Figure 14. Schematic illustration of the photocatalytic and antibacterial mechanisms of ZnO nanoparticles synthesized using *Madhuca longifolia* flower extract

Table 2. Comparative analysis of the photocatalytic performance of biosynthesized ZnO nanoparticles with previously reported ZnO-based catalysts for the degradation of Eosin Blue dye

Sr. No.	Plant Extract Used for ZnO Synthesis	Key Characteristics of Synthesized ZnO	Degradation Efficiency (Eosin Blue)	Degradation Time	References
1	*Mangifera indica* gum (Er-doped ZnO)	Er-doped ZnO, potential for enhanced photocatalysis due to electron traps.	81.2% (Eosin Y)	120 min (UV irradiation)	[69]
2	Pistachio skin extract	Crystalline, spherical morphology, band gap ~3.17 eV.	Good to excellent (Eosin Y)	Not specified (under UV & visible radiation)	[70]
3	*Ambrosia ambrosioides* leaf/root extract	Contains organic components and has high thermal stability.	(Implied high efficiency, similar to other dyes degraded)	Not specified for Eosin, but other dyes ~60-140 min (UV irradiation)	[71]
4	*Panax* extract (e.g., *Panax ginseng*)	Flower-shaped ZnO nanoflowers (ZnO/QNF) have a high surface area.	>99% (Eosin Y, for 15 mg/L)	90 min (UV illumination)	[72]
5	Sea buckthorn fruit (SBT)	Flower-shaped ZnO nanoflower (ZnO/NF).	Full degradation (Eosin Y)	~1/3 of the original photocatalyst time (UV radiation)	[73]
6	*Madhuca longifolia* flower extract	Sphereical ZnO	97% (Eosin Blue 10 mg/L at pH=8)	90 min (Sunlight)	This work

Beyond photocatalysis, the biogenic ZnO NPs demonstrate potent antibacterial activity against both Gram-positive (*Bacillus cereus*, *Staphylococcus saprophyticus*) and Gram-negative (*Escherichia coli*, *Salmonella typhimurium*) bacterial strains. This broad-spectrum antimicrobial effect arises from synergistic mechanisms. Firstly, the ROS generated on the nanoparticle surface induces oxidative stress within bacterial cells, leading to lipid peroxidation, protein oxidation, and DNA damage. Secondly, the electrostatic attraction between the positively charged ZnO NP surface and negatively charged bacterial membranes disrupts membrane integrity, increasing permeability and causing leakage of essential intracellular constituents. Lastly, the controlled release of Zn^{2+} ions from the nanoparticles further enhances bactericidal activity by interfering with enzymatic functions, inhibiting DNA replication, and promoting intracellular ROS formation [68]. The phytochemical capping agents derived from *M. longifolia* not only stabilize the nanoparticles but may also modulate surface charge and ion release, optimizing the interaction between ZnO NPs and bacterial membranes. This dual

functionality efficient photocatalysis and robust antibacterial performance demonstrates that plant-mediated ZnO nanoparticles are promising candidates for eco-friendly wastewater treatment and antimicrobial applications, combining sustainability with multifunctional efficiency.

3.10. Compression of ZnO NP's for the degradation of Eosin dye

Table 2 presents a comparative summary of various plant-extract-mediated ZnO nanoparticles reported for the photocatalytic degradation of Eosin dye. The data highlight the critical role of different plant-derived biomolecules in dictating the morphology, crystallinity, and photocatalytic efficiency of ZnO nanostructures. Distinct phytochemicals present in each extract act as natural reducing, capping, and stabilizing agents, thereby influencing the nucleation kinetics, particle size, and surface defect density of the resulting nanoparticles.

A clear variation in degradation efficiency and reaction time is observed among the different plant-mediated systems, emphasizing the dependence of photocatalytic performance on the biochemical composition of the precursor extracts. Notably, ZnO nanoparticles synthesized using Panax ginseng and Madhuca longifolia flower extracts exhibit superior degradation efficiencies and shorter reaction times compared to those derived from other botanical sources. This enhanced activity is attributed to the abundance of phenolic and flavonoid compounds, which promote smaller particle sizes, increased surface reactivity, and improved charge separation dynamics. Overall, the comparative analysis underscores the versatility and potential of green synthesis approaches in tailoring the physicochemical and catalytic properties of ZnO nanostructures. Such bio-assisted strategies not only provide environmentally sustainable routes for nanomaterial fabrication but also open new pathways for designing high-performance photocatalysts for dye degradation and other environmental remediation applications.

3.11. Limitations and Future Work

While the present study successfully demonstrates the effectiveness of green-synthesized ZnO nanoparticles using *Madhuca longifolia* flower extract, several limitations merit consideration. The current investigation focuses on a single, undoped ZnO system, which, although effective, could benefit from further enhancement through metal or non-metal doping and the development of ZnO-based heterostructures. Such modifications are expected to extend light absorption into the visible region, suppress electron–hole recombination, and thereby improve overall photocatalytic efficiency. Moreover, the experiments were performed at a laboratory scale, and questions related to process scalability, long-term operational stability, and cost-effectiveness must be systematically addressed before translating this approach to industrial or field-scale applications. Future studies should therefore emphasize process optimization, life-cycle assessment, and regeneration efficiency to ensure environmental and economic sustainability.

In addition to photocatalytic dye degradation, the synthesized ZnO nanoparticles exhibit promising antibacterial activity, suggesting their potential in biomedical applications, such as antimicrobial coatings, wound dressings, and disinfectant formulations. Similarly, their robust photocatalytic performance under solar irradiation positions them as strong candidates for wastewater treatment and environmental remediation.

Future research efforts will focus on the design of doped or composite ZnO-based photocatalysts, optimization of green synthesis parameters for large-scale production, and exploration of interdisciplinary applications that bridge environmental nanotechnology and biomedical science. These directions aim to advance the sustainable utilization of bio-fabricated nanomaterials for real-world technological applications.

4. Conclusion

The present study successfully demonstrates a facile, sustainable, and eco-friendly approach for the synthesis of zinc oxide (ZnO) nanoparticles via a green hydrothermal method utilizing *Madhuca longifolia* flower extract as a natural bioreductant and stabilizing agent. Comprehensive physicochemical analyses, including XRD, SEM-EDS, TEM, FT-IR, and UV–vis spectroscopy, confirmed the formation of well-crystallized ZnO nanoparticles with an average crystallite size of 17–20 nm and a direct band gap of 3.21 eV, indicative of their semiconducting nature and optical purity. The biosynthesized ZnO nanoparticles exhibited remarkable photocatalytic performance, achieving efficient degradation of Eosin Blue dye under natural solar irradiation, thereby validating their potential for environmental remediation applications. In addition, the nanoparticles demonstrated broad-spectrum antibacterial activity against both Gram-positive and Gram-negative bacteria, underscoring their promise as effective antimicrobial agents. The presence of bioactive phytochemicals in the *Madhuca longifolia* extract contributed not only to particle stabilization and size control but also enhanced the overall surface reactivity and biocompatibility of the nanomaterial. Importantly, this green synthetic route aligns with the principles of sustainable nanotechnology, offering a low-cost, non-toxic, and renewable alternative to conventional chemical synthesis methods. The findings highlight the

multifunctional potential of *Madhuca longifolia*-mediated ZnO nanoparticles for dual applications in photocatalytic pollutant degradation and biomedical disinfection systems. Future research will focus on mechanistic elucidation, doping or composite formation to improve light utilization, and scalability assessments to facilitate the translation of this environmentally benign process to industrial and real-world applications.

Acknowledgments

The authors sincerely acknowledge the continuous encouragement and infrastructural support provided by Sandip University, Nashik, the Principal of K. V. N. Naik Arts, Commerce and Science College, Nashik, Pukyong National University, Busan, South Korea, and ASPIRE Research Grant, SPPU, Pune, for facilitating this research through access to laboratory and other resources. The authors are also grateful to the Central Instrumentation Facility (CIF), Savitribai Phule Pune University (SPPU), Pune, for extending support in characterization studies such as FT-IR, SEM, EDS, XRD, and ZPC analysis. We further acknowledge IIT Bombay for assistance with TEM analysis and Pukyong National University, Busan, South Korea, for providing the necessary facilities and expertise for antimicrobial studies. The collaborative support from these institutions has been invaluable in completing the present work.

Funding
This research did not receive any specific grant from funding agencies in the public, commercial, or not-for-profit sectors. The work was carried out with institutional support and collaborative facilities.

Conflict of Interest
The authors declare that they have no known competing financial interests or personal relationships that could have appeared to influence the work reported in this paper.

Data Availability
The datasets generated during and/or analysed during the current study are available from the corresponding author on reasonable request.

References

[1] T.A. Khattab, M.S. Abdelrahman, and M. Rehan. *Environ. Sci. Pollut. Res.*, **27** (2020) 3803–3818. https://doi.org/10.1007/s11356-019-07137-z

[2] T. Islam, M.R. Repon, T. Islam, Z. Sarwar, and M.M. Rahman. *Environ. Sci. Pollut. Res.*, **30** (2023) 9207–9242. https://doi.org/10.1007/s11356-022-24398-3

[3] D. Thapliyal, K. Tewari, S. Verma, C.K. Bhargava, P. Sen, A. Mehra, and R.K. Arya. *Func. Coat. Biomed. Energ. Environ. Applicat.*, (2024) 1–30. https://doi.org/10.1002/9781394263172.ch1

[4] E.S. Okeke, K.I. Chukwudozie, R. Nyaruaba, R.E. Ita, A. Oladipo, O. Ejeromedoghene, and C.O. Okoye. *Environ. Sci. Pollut. Res.*, **29** (2022) 69241–69274. https://doi.org/10.1007/s11356-022-22319-y

[5] T. Miyazawa, M. Itaya, G.C. Burdeos, K. Nakagawa, and T. Miyazawa. *Int. J. Nanomed.*, **16** (2021) 3937–3999. https://doi.org/10.2147/IJN.S298606

[6] K. Gold, B. Slay, M. Knackstedt, and A.K. Gaharwar. *Adv. Therap.*, **1** (2018) 1700033. https://doi.org/10.1002/adtp.201700033

[7] N. Ahmad, S.N.A. Bukhari, M.A. Hussain, H. Ejaz, and M.U. Munir. *RSC Adv.*, **14** (2024): 13535–13564. https://doi.org/10.1039/D4RA00631C

[8] I. Ahmad, Y. Zou, J. Yan, Y. Liu, S. Shukrullah, M.Y. Naz, and N.R. Khalid. *Adv. Colloid Interface Sci.*, **311** (2023) 102830. https://doi.org/10.1016/j.cis.2022.102830

[9] Z. Wang, Z. Lin, S. Shen, W. Zhong, and S. Cao. *Chin. J. Catal.*, **42** (2021) 710–730. https://doi.org/10.1016/S1872-2067(20)63698-1

[10] D. Durgalakshmi, R.A. Rakkesh, S. Rajendran, and M. Naushad. *Green Photocatalysts*, (2020) 1–24. https://doi.org/10.1007/978-3-030-15608-4_1

[11] M. Guli, E.T. Helmy, J. Schneider, G. Lu, and J.H. Pan. *Top. Curr. Chem.*, **380** (2022) 39. https://doi.org/10.1007/s41061-022-00394-6

[12] A. Iqbal, A. Yusaf, M. Usman, T.H. Bokhari, and A. Mansha. *Int. J. Environ. Anal. Chem.*, **104** (2024) 5503–5537. https://doi.org/10.1080/03067319.2022.2125312

[13] P. Kumari, A. Srivastava, R.K. Sharma, D. Sharma, and S.K. Srivastava. *Nanomaterials for Innovative Energy Systems and Devices*, (2022) 173–241. https://doi.org/10.1007/978-981-19-0553-7_6

[14] A.A. Ansari, R. Lv, S. Gai, A.K. Parchur, P.R. Solanki, Z.A. Ansari, and M.M. Tavakoli. *Coord. Chem. Rev.*, **515** (2024) 215942. https://doi.org/10.1016/j.ccr.2024.215942

[15] A. Rasool, S. Kiran, T. Gulzar, S. Abrar, A. Ghaffar, and M. Shahid. *J. Cleaner Prod.*, **398** (2023) 136616. https://doi.org/10.1016/j.jclepro.2023.136616

[16] M.T. Noman, N. Amor, and M. Petru. *Crit. Rev. Solid State Mater. Sci.*, **47** (2022) 99–141. https://doi.org/10.1080/10408436.2020.1847030

[17] C.B. Ong, L.Y. Ng, and A.W. Mohammad. *Renew. Sust. Energy Rev.*, **81** (2018) 536–551. https://doi.org/10.1016/j.rser.2017.08.020

[18] K. Bachhav and A.S. Garde. *Mater. Today: Proc.*, **83** (2023) 2036–2043. https://doi.org/10.1016/j.matpr.2023.08.269

[19] A.R. Bhapkar and S. Bhame. *J. Environ. Chem. Eng.*, **12** (2024) 112553. https://doi.org/10.1016/j.jece.2024.112553

[20] T. Mohapatra, M. Agrawal, and P. Ghosh. *Chem. Eng. J.*, **465** (2023) 146941. https://doi.org/10.1016/j.cej.2023.146941

[21] A. Mengstu, S. Esubalew, L. Abate, R.K.B.A. Husen, and A. Bachheti. *Secondary Metabolites from Medicinal Plants*, (2023) 35–52. https://doi.org/10.25258/ijddt.14.3.20

[22] M. Jothibas, E. Paulson, S. Srinivasan, and B.A. Kumar. *Surf. Interfaces*, **29** (2022) 101734. https://doi.org/10.1016/j.surfin.2022.101734

[23] D. Maity and U. Gupta. *Nanoscale*, **14** (2022) 13950–13989. https://doi.org/10.1039/D2NR03944C

[24] R.A. Banjara, A. Kumar, R. Aneshwari, M.L. Satnami, and S.K. Sinha. *Environ. Nanotechnol. Monit. Manage.*, **22** (2024) 100988. https://doi.org/10.1016/j.enmm.2024.100988

[25] U. Shanker, V. Jassal, M. Rani, and B.S. Kaith. *Int. J. Environ. Anal. Chem.*, **96** (2016) 801–835. https://doi.org/10.1080/03067319.2016.1209663

[26] P. Jamdagni, P. Khatri, and J.S. Rana. *J. King Saud Univ.–Sci.*, **30** (2018) 168–175. https://doi.org/10.1016/j.jksus.2016.10.002

[27] H. Kumar, K. Bhardwaj, K. Kuča, A. Kalia, E. Nepovimova, and R. Verma. *Nanomaterials*, **10** (2020) 766. https://doi.org/10.3390/nano10040766

[28] C.A. Aydin Acar, M.A. Gencer, S. Pehlivanoglu, S. Yesilot, and S. Donmez. *Int. Wound J.*, **21** (2024) e14413. https://doi.org/10.1111/iwj.14413

[29] S. Yildirimcan, S. Erat, S. Cetinkaya, and M. Aycibin. *Phys. Lett. A*, **516** (2024) 129640. https://doi.org/10.1016/j.physleta.2024.129640

[30] I.Y. Bouderbala, A. Guessoum, S. Rabhi, O. Bouhlassa, and I.E. Bouras. *Appl. Phys. A*, **130** (2024) 205. https://doi.org/10.1007/s00339-024-07366-1

[31] Y.S. Chan, J.S.L. Ng, and W.Y.W.A. Rahman. *Nanotechnol. Rev.*, **14** (2025) 20250157. https://doi.org/10.1515/ntrev-2025-0157

[32] T.S. Aldeen, H.E.A. Mohamed, and M. Maaza. *J. Phys. Chem. Solids*, **160** (2022) 110313. https://doi.org/10.1016/j.jpcs.2021.110313

[33] S. Yadav, T. Nadar, J. Lakkakula, and N.S. Wagh. *Biogenic Nanomaterials for Environmental Sustainability: Principles, Practices, and Opportunities*, (2024) 147–188. https://doi.org/10.1007/978-3-031-45956-6_6

[34] A. Gouthaman, A. Gnanaprakasam, V.M. Sivakumar, M. Thirumarimurugan, A. Mohamed, and R.S. Azarudeen. *J. Hazard. Mater.*, **373** (2019) 493–503. https://doi.org/10.1016/j.jhazmat.2019.03.105

[35] T. Romih, A. Jemec, S. Novak, L. Vaccari, P. Ferraris, M. Šimon, and M. Kos. *Nanotoxicology*, **10** (2016) 462–470. https://doi.org/10.3109/17435390.2015.1078853

[36] M. MuthuKathija, M.S.M. Badhusha, and V. Rama. *Appl. Surf. Sci. Adv.*, **15** (2023) 100400. https://doi.org/10.1016/j.apsadv.2023.100400

[37] Chan Y.B., Aminuzzaman M., Win Y.F., Djearamane S., Wong L.S., Guha S.K., Almohammadi H., Akhtaruzzaman M., Tey L.H. *Catalysts,* **14** (2024) 486. https://doi.org/10.3390/catal14080486

[38] E.T. Cheah, N.N.R. Mohamad, N.S.A. Hamid, T.M.Y.T.M. Zawawi, A.S.A. Jaafar, and M.R.M.N. Che-Osman. *Green Process. Synth.*, **13** (2024) 20240246. https://doi.org/10.1515/gps-2024-0246

[39] S.F. Elhabal, N. Abdelaal, S.A.K.S. Al-Zuhairy, M.F.M. Elrefai, A.M.E. Hamdan, M.M. Khalifa, and M.A. El-Nabarawi. *Int. J. Nanomed.*, **19** (2024) 3045–3070. https://doi.org/10.2147/IJN.S455270

[40] S.G. Shinde, M.P. Patil, G.D. Kim, and V.S. Shrivastava. *J. Inorg. Organomet. Polym. Mater.*, **30** (2020) 1141–1152. https://doi.org/10.1007/s10904-019-01273-2

[41] I.G. Shitu, K.K. Katibi, A. Muhammad, I.M. Chiromawa, R.A. Tafida, A.A. Amusa, and S. Babani. *Opt. Quantum Electron.*, **56** (2024) 266. https://doi.org/10.1007/s11082-023-05867-6

[42] V. Mohanraj, R. Jayaprakash, J. Chandrasekaran, R. Robert, and P. Sangaiya. *Mater. Sci. Semicond. Process.*, **66** (2017) 131–139. https://doi.org/10.1016/j.mssp.2017.04.006

[43] Lim S.C.Y., Koh M.X., Chan Y.B., Djearamane S., Yeh C.S., Chen C.H., Wong L.S., Tey L.H. *J. Taiwan Inst. Chem. Eng.,* **150** (2025) 106368. https://doi.org/10.1016/j.jtice.2025.106368

[44] C. Wu, T. Zhang, B. Ji, Y. Chou, and X. Du. *Cellulose*, **31** (2024) 1–16. https://doi.org/10.1007/s10570-024-05914-9

[45] I.S. Saputra, E. Nurfani, A.G. Fahmi, A.H. Saputro, D.O.B. Apriandanu, D. Annas, and Y. Yulizar. *Vacuum*, **227** (2024) 113434. https://doi.org/10.1016/j.vacuum.2024.113434

[46] A. Zyoud, A.H. Zyoud, S.H. Zyoud, H. Nassar, S.H. Zyoud, N. Qamhieh, A. Hajamohideen, and H.S. Hilal. *Environ. Sci. Pollut. Res.*, **30** (2023) 68435–68449. https://doi.org/10.1007/s11356-023-27318-1

[47] T.J. Al-Musawi, P. Rajiv, N. Mengelizadeh, F.S. Arghavan, and D. Balarak. *J. Mol. Liq.*, **337** (2021) 116470. https://doi.org/10.1016/j.molliq.2021.116470

[48] S. Sasidharan, S.J.T.T. Lim, and W.Y.W.A. Rahman. *Food Packag. Shelf Life*, **43** (2024) 101298. https://doi.org/10.1016/j.fpsl.2024.101298

[49] T. Zhang, Y. Yang, J. Gao, X. Li, H. Yu, N. Wang, and P. Du. *Sep. Purif. Technol.*, **240** (2020) 116575. https://doi.org/10.1016/j.seppur.2020.116575

[50] X. Zou, T. Zhou, J. Mao, and X. Wu. *Chem. Eng. J.*, **257** (2014) 36–44. https://doi.org/10.1016/j.cej.2014.07.048

[51] L. Li, X. Niu, D. Zhang, X. Ye, Z. Zhang, Q. Liu, and L. Ding. *Water Res.*, **247** (2024) 121842. https://doi.org/10.1016/j.watres.2024.121842

[52] S.N. Malik, P.C. Ghosh, A.N. Vaidya, and S.N. Mudliar. *J. Water Process Eng.*, **35** (2020) 101193. https://doi.org/10.1016/j.jwpe.2020.101193

[53] A. Ranjbari, J. Yu, J. Kim, J. Kim, M. Park, K.H. Kim, and P.M. Heynderickx. *Appl. Surf. Sci.*, **659** (2024) 159867. https://doi.org/10.1016/j.apsusc.2024.159867

[54] H. Jabeen, S. Shaukat, and H.M.A.U. Rahman. *J. Mol. Liq.*, **395** (2024) 123783. https://doi.org/10.1016/j.molliq.2023.123783

[55] A. Batool, R. Munir, N. Mushtaq, and S. Noreen. *J. Sol-Gel Sci. Technol.*, **112** (2024) 240–261. https://doi.org/10.1007/s10971-024-06490-x

[56] A. Serouti, L.S. Eddine, S. Meneceur, G.G. Hasan, H.A. Mohammed, C. Salmi, and J.A.A. Abdullah. *Arab. J. Sci. Eng.*, **49** (2024) 753–764. https://doi.org/10.1007/s13369-023-08495-0

[57] F. Guo, X. Huang, Z. Chen, H. Sun, and L. Chen. *Chem. Eng. J.*, **395** (2020) 125118. https://doi.org/10.1016/j.cej.2020.125118

[58] O. Bechambi, S. Sayadi, and W. Najjar. *J. Ind. Eng. Chem.*, **32** (2015) 201–210. https://doi.org/10.1016/j.jiec.2015.08.019

[59] A.K. Wanjari, M.P. Patil, U.E. Chaudhari, V.N. Gulhane, G.D. Kim, and A.T. Kiddane. *Part. Sci. Technol.*, **40** (2022) 1033–1040. https://doi.org/10.1080/02726351.2022.2056552

[60] K.R. Raghupathi, R.T. Koodali, and A.C. Manna. *Langmuir*, **27** (2011): 4020–4028. https://doi.org/10.1021/la104825u

[61] M.P. Patil, J.O. Kim, Y.B. Seo, M.J. Kang, and G.D. Kim. *J. Life Sci.*, **31** (2021) 862–872. https://doi.org/10.5352/JLS.2021.31.9.862

[62] M. Premanathan, K. Karthikeyan, K. Jeyasubramanian, and G. Manivannan. *Nanomed.: Nanotechnol. Biol. Med.*, **7** (2011): 184–192. https://doi.org/10.1016/j.nano.2010.10.001

[63] R.K. Dutta, B.P. Nenavathu, M.K. Gangishetty, and A.V.R. Reddy. *Colloids Surf. B: Biointerfaces*, **94** (2012) 143–150. https://doi.org/10.1016/j.colsurfb.2012.01.046

[64] W.R. Li, X.B. Xie, Q.S. Shi, H.Y. Zeng, Y.S. Ou-Yang, and Y.B. Chen. *Appl. Microbiol. Biotechnol.*, **85** (2010) 1115–1122. https://doi.org/10.1007/s00253-009-2159-5

[65] J. Sawai. *J. Microbiol. Methods*, **54** (2003) 177–182. https://doi.org/10.1016/S0167-7012(03)00037-X

[66] N. Jones, B. Ray, K.T. Ranjit, and A.C. Manna. *FEMS Microbiol. Lett.*, **279** (2008) 71–76. https://doi.org/10.1111/j.1574-6968.2007.01012.x

[67] M.P. Patil, R.D. Singh, P.B. Koli, K.T. Patil, B.S. Jagdale, A.R. Tipare, and G.-D. Kim. *Microb. Pathog.*, **121** (2018) 184–189. https://doi.org/10.1016/j.micpath.2018.05.040

[68] R.S. Shinde, R.A. More, V.A. Adole, P.B. Koli, T.B. Pawar, B.S. Jagdale, B.D. Desale, and Y.P. Sarnikar. *Curr. Res. Green Sustain. Chem.*, **4** (2021) 100138. https://doi.org/10.1016/j.crgsc.2021.100138

[69] Silva M.C., Castro-Lopes S., Jerônimo A.G., Barbosa R., Lins A., Trigueiro P., Viana B.C., Araujo F.P., Osajima J.A., Peña-Garcia R.R. *Molecules,* **29** (2024) 391. https://doi.org/10.3390/molecules29020391

[70] Aldeen T.S., Mohamed H.E.A., Maaza M. *J. Phys. Chem. Solids,* **160** (2022) 110313. https://doi.org/10.1016/j.jpcs.2021.110313

[71] Zewde D., Geremew B. *Environ. Pollut. Bioavail.,* **34** (2022) 224–235. https://doi.org/10.1080/26395940.2022.2069618

[72] L. Kaliraj, S. Anbuvannan, S.R. Kumar, K. Prabu, and P.S. Sivakumar. *J. Photochem. Photobiol. B: Biol.*, **199** (2019) 111588. https://doi.org/10.1016/j.jphotobiol.2019.111588

[73] E.J. Rupa, L. Kaliraj, S. Abid, D.-C. Yang, and S.-K. Jung. *Nanomaterials*, **9** (2019) 1692. https://doi.org/10.3390/nano9121692